

Projectile fragmentation reactions and production of nuclei near the neutron drip-line

M. Notani^{1,*}, H. Sakurai^{2,†}, N. Aoi³, H. Iwasaki^{2,‡}, N. Fukuda³, Z. Liu^{3,§}, K. Yoneda³,
 H. Ogawa³, T. Teranishi^{1,¶}, T. Nakamura⁴, H. Okuno³, A. Yoshida³, Y. Watanabe^{3,**},
 S. Momota⁵, N. Inabe³, T. Kubo³, S. Ito³, A. Ozawa³, T. Suzuki³, I. Tanihata^{3,††}, and M. Ishihara³

¹*Center for Nuclear Study, University of Tokyo (CNS) RIKEN Campus, 2-1 Hirosawa, Wako, Saitama 351-0198, Japan*

²*Department of Physics, University of Tokyo, 7-3-1 Hongo, Bunkyo, Tokyo 113-0033, Japan*

³*RIKEN (The Institute of Physical and Chemical Research), 2-1 Hirosawa, Wako, Saitama 351-0198, Japan*

⁴*Department of Applied Physics, Tokyo Institute of Technology,
 2-12-1 Oh-okayama, Meguro-ku, Tokyo 152-8551, Japan and*

⁵*Department of Intelligent Mechanical Systems Engineering,
 Kochi University of Technology, Tosayamada-cho, Kochi 782, Japan*

(Dated: September 11, 2018)

The reaction mechanism of projectile fragmentation at intermediate energies has been investigated observing the target dependence of the production cross sections of very neutron-rich nuclei. Measurement of longitudinal momentum distributions of projectile-like fragments within a wide range of fragment mass and its charge was performed using a hundred-MeV/n ⁴⁰Ar beam incident on Be and Ta targets. By measurement of fragment momentum distribution, a parabolic mass dependence of momentum peak shift was observed in the results of both targets, and a phenomenon of light-fragment acceleration was found only in the Be-target data. The analysis of production cross sections revealed an obvious enhancement of the target dependence except target size effect when the neutron excess is increased. This result implies the breakdown of factorization (BOF) of production cross sections for very neutron-rich nuclei near the drip line.

PACS numbers: 25.70.Mn, 25.70.-z, 27.20.+n, 27.30.+t, 27.40.+z

I. INTRODUCTION

During these two decades, unstable nuclear physics has become one of the most interesting fields of nuclear physics. Nuclear fragmentation of heavy-ion beams is utilized for producing secondary beams of unstable nuclei far from β -stability. For designing experiments with the secondary beams, a good knowledge of production cross sections is essential. To deduce the production cross sections relevantly, an empirical parametrization of fragmentation cross sections (EPAX) is widely used in simulation programs for projectile-fragment separators [1, 2, 3]. For consideration of reaction mechanism, fragmentation models based on abrasion-ablation scheme (AA models) are often applied to estimate the production cross sections.

With the recent development of heavy-ion accelerators, the number of accessible nuclei lying far from β -stability line has been increasing. An example has been shown by the experimental findings of particle stability of ³¹F [4], ^{31,34}Ne [5, 6], ³⁷Na [6], ^{37,38}Mg [5, 7], ^{40,41}Al [7], and

⁴³Si [6], as the most neutron-rich nuclei so far identified for the $Z=9-14$ elements. For the new isotope-search experiment, the accuracy to predict the production cross section of neutron-rich nuclei near the drip line is very important to discuss the particle stability of them. However, the predictive power of the EPAX parametrization and AA models is not strong enough for specific very neutron-rich nuclei [8]. For instance, although tantalum is often experimentally used as a production target in order to earn the better yield of these nuclei, the target dependence of production cross sections is not taken into account in these models. Instead, we first determined the production cross sections for the observed isotopes, which were then used to estimate the production cross sections and the expected yields for the non-observed isotopes. Therefore, to enhance predictive powers for production cross sections, deeply understanding reaction mechanism as well as observing systematic behaviors of production cross sections are necessary.

The validity of the EPAX parametrization and AA models has been mainly verified for medium and heavy mass fragments via multi-GeV high-energy fragmentation reactions. The EPAX formula has been also used for the intermediate-energy experiments (several tens A MeV) since the formula can reproduce reasonably well even at intermediate energies the production cross sections of stable and unstable nuclei near the β -stability line. A target dependence of fragment-production cross sections in relativistic heavy-ion collisions is limited only by taking account of the nuclear-size effect [9]. However, the recent experiments show that the production yields of nuclei far from stability line are quite different from

*Present address: Physics Division, Argonne National Laboratory, U.S.A.

†Present address: RIKEN, Japan

‡Present address: IPN, F-91406 Orsay Cedex, France

§Present address: University of Surrey, U.K.

¶Present address: Department of Physics, Kyushu University, Japan

**Present address: High Energy Accelerator Research Organization (KEK), Japan

††Present address: TRIUMF, Canada

the prediction of EPAX formula, and strongly dependent on the N/Z ratio of the target [10]. It is of great interest whether the cross sections measured with different targets factorize in projectile fragmentation at intermediate energies.

In order to confirm the validity of factorization, a careful measurement of fragment momentum distribution is necessary for precise determination of the production cross sections. At relativistic energies, the shape of momentum distribution for an isotope was found to be a Gaussian function [11] and the width was well understood with a statistical model [12]. On the other hand, the momentum distribution of fragments produced at intermediate energies has an asymmetric shape with a tail at low momentum side. A theoretical attempt was made to reproduce the asymmetric shape, by taking into account nucleon flows between projectile and target in the collision time [13]. In this model, stochastic nucleon transfers using a Monte Carlo method and sequential evaporation were taken into account. This model can reproduce the low-momentum-side tails, however, due to a large friction force, the whole of predicted distributions are shifted toward the low momentum side much larger than the observed. This discrepancy of momentum distributions affords a large ambiguity to evaluate the production cross section from the measured yield of fragments. In addition, the measurement for very neutron-rich nuclei has been performed using very thick targets to earn the yields, so far. As distortions of momentum distributions due to target thickness, the momentum distributions of fragments cannot be obtained from these data clearly. Therefore, the measurement of momentum distribution of very neutron-rich nuclei has become important.

In the present work, we focus on the target dependence of momentum distribution of projectile-like fragment (PLF) produced by nuclear fragmentation reactions at an intermediate energy. To investigate the target dependence of the production cross sections systematically, we used two production targets of Be and Ta. To avoid distortions of momentum distributions due to the target thickness, we prepared relatively thin targets. We performed the experiment with the RIKEN-RIPS to eliminate the primary beam and to collect the projectile-like fragments. The data of this experiment were taken in a wide range for fragment mass including very neutron-rich side ($N/Z_f \approx 3$) toward the neutron drip-line and light mass ($A_f \geq 3$), with a good statistics for momentum-distribution tails.

In the following, we first describe the experimental setup and procedure in Sec. II. In Sec. III, the analysis of the data is described. In Sec. IV, the experimental results are described, where the observed momentum distributions of fragments, the momentum peak shift, the high- and low-momentum side widths, and the production cross sections are presented in terms of target dependence. Based on the results, we discuss the prefragment production mechanism in projectile fragmentation reactions.

II. EXPERIMENTAL SETUP AND PROCEDURE

The projectile fragmentation experiment using a ^{40}Ar beam was performed at the RIKEN Accelerator Research Facility. The measurement of momentum distributions of projectile-like fragments was carried out with the projectile fragment separator, RIPS [14]. The $^{40}\text{Ar}^{17+}$ beam accelerated by the ring cyclotron with energies up to 90A MeV and 94A MeV irradiated a 95-mg/cm² thick ^9Be target and a 17-mg/cm² thick ^{nat}Ta target, respectively.

The primary beam intensity was monitored for normalization of fragment yields to obtain the momentum distribution. A plastic telescope consisted of three plastic scintillators with a size of $50 \times 50 \times 0.5$ mm³ was placed at a backward angle of 135 degrees and at a distance of 0.5 m from the target position. The plastic detectors counted yield rates of light particles produced with nuclear reactions at the production target. The three photomultiplier tubes (PMTs) were mounted on the plastic scintillators one-by-one. The counting rate of triple coincidence was used to monitor the primary beam. The primary beam intensity was measured with the indirect method of plastic counters calibrated by a Faraday cup. By changing the primary-beam intensity which ranges from 10^{-4} to 1.0 of the full beam intensity, the calibration data were taken. The systematic error of the beam monitor was estimated to be 7%.

The RIPS was used as a doubly achromatic spectrometer. Projectile fragments produced at the production target and emitted at 0° were collected and transported to a double achromatic focal plane (F2). The momentum acceptance was set to be $\Delta p/p=1\%$ at a momentum dispersive focal plane (F1) where left and right slits formed the rectangle window of momentum acceptance. The angular acceptance was set with a square window formed by four slits (upper, lower, left and right), which were placed at the behind of the production target. The θ and ϕ angular acceptances were 25 mrad, which is narrower than the width of angular distribution of fragments in r.m.s. We use the constant value of 6.25×10^{-1} msr as the solid angle of $\Delta\Omega$.

Momentum distributions of fragments were measured at 23 settings of magnetic rigidity ($B\rho$) over a range of 2.520–4.068 Tm using ^9Be target. In the case of ^{181}Ta target, the measurement of momentum distribution for each fragment was performed at 31 magnet settings as same as Be case. When the magnetic field was changed for each run, the F2 image of secondary beam was measured by means of a parallel-plate avalanche counter (PPAC) [15] to confirm transmission, and the x-position of the beam at F2 was corrected to center precisely by tuning the D2 field. The beam position was monitored with an accuracy of 1 mm. The systematic error of magnetic rigidity was about 3×10^{-4} from the ratio of 1 mm to 3.6 m. The difference between D1 and D2 magnetic fields was less than 0.05%.

The identification of fragments was carried out event-

by-event by means of measurement of time of flight (TOF) and energy deposit (ΔE) for each fixed $B\rho$ run with the 1% momentum slit. According to an estimation of charge state distribution [16], all fragments in flight are fully stripped ($Q \cong Z$). Under this assumption, the particle identification can be performed on the basis of the relations:

$$B\rho \propto \frac{A}{Z}\beta \quad (1)$$

$$\Delta E \propto \left(\frac{Z}{\beta}\right)^2 \quad (2)$$

$$\beta \propto \frac{1}{TOF}, \quad (3)$$

where A and Z are mass number and atomic number, respectively.

The detectors of two 0.5-mm thick surface-barrier-type silicon counters (SSD1, SSD2) and a 0.5-mm thick plastic scintillation counter (PL) were installed for the ΔE and TOF measurement at F2. To use two silicon detectors allowed us to deduce Z number of the fragment independently, and to take correlations between them to achieve good S/N ratio.

Both SSD1 and SSD2 have 48 mm \times 48 mm sensitive area which is wide enough to accept all particles reaching to F2 where FWHM of the beam profile is 6 mm. Two photomultiplier tubes (PMTs) were mounted on both sides of PL (Left and Right). A timing of PL was determined with an average of the signals from the Left and Right.

The TOF of each fragment over 21.3-m flight path between the production target and the F2 was determined from the difference of timing signals between RF signal of the cyclotron and the PL timing. The TOF resolution was measured with a faint beam to be 0.27 ns (r.m.s.), which included the timing jitter of RF signal (~ 0.09 ns). Thus, the intrinsic resolution for PMT was estimated to be 0.18 ns.

III. DATA ANALYSIS

In this section we describe the procedures of the data analysis, fitting of momentum distributions, and evaluation of the production cross sections.

A. Particle identification

Figure 1 shows a two-dimensional plot versus ΔE in SSD1 for one $B\rho$ setting using the Be target. A rejection of the background events was carried using a correlation gate between SSD1 and SSD2. By use of the $3\text{-}\sigma$ gate by two SSDs, we achieved the particle identification of fragments with low background events. Fragment yields were obtained by counting the isotopes from the particle identification. Figure 2 shows the Z - and A/Z -projection

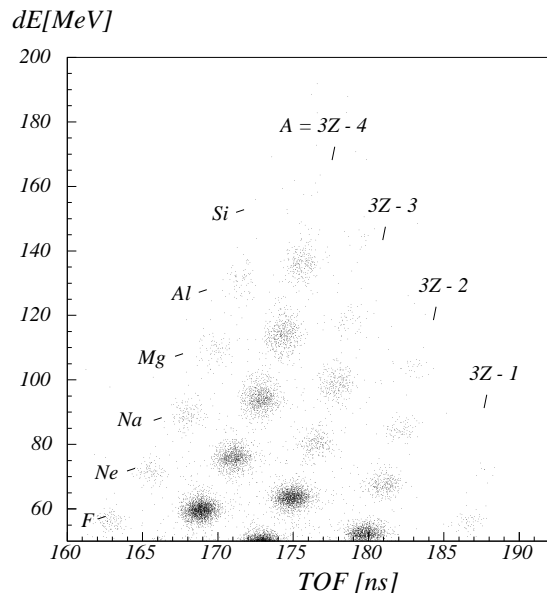


FIG. 1: Particle identification in the dE -TOF plane at $B\rho = 3.708$ Tm with the Be target.

of the particle identification at $B\rho = 2.523$ Tm setting using the Be target. The counting gate of isotopes was a rectangle region with $\pm 3\text{-}\sigma$ of the resolution σ (r.m.s.) for Z and A/Z .

In the data acquired using the Be target, the analyzed isotopes were ${}^6\text{-}9\text{Li}$, ${}^7\text{-}12\text{Be}$, ${}^{10}\text{-}15\text{B}$, ${}^{11}\text{-}18\text{C}$, ${}^{13}\text{-}21\text{N}$, ${}^{15}\text{-}24\text{O}$, ${}^{17}\text{-}27\text{F}$, ${}^{19}\text{-}29\text{Ne}$, ${}^{21}\text{-}32\text{Na}$, ${}^{23}\text{-}34\text{Mg}$, ${}^{25}\text{-}36\text{Al}$, ${}^{27}\text{-}38\text{Si}$, ${}^{29}\text{-}39\text{P}$, ${}^{33}\text{-}38\text{S}$, ${}^{36}\text{-}39\text{Cl}$, and ${}^{39}\text{Ar}$. Most of these isotopes are neutron-rich ones. It should be noted that the ${}^{36}\text{Al}$, ${}^{37,38}\text{Si}$, and ${}^{38,39}\text{P}$ isotopes analyzed have neutron numbers larger than the projectile ($N \geq 23$), which are produced through neutron pick-up process. We analyzed from the Ta-target data for ${}^6\text{-}8\text{Li}$, ${}^9\text{-}11\text{Be}$, ${}^{10}\text{-}14\text{B}$, ${}^{11}\text{-}17\text{C}$, ${}^{13}\text{-}19\text{N}$, ${}^{15}\text{-}21\text{O}$, ${}^{17}\text{-}24\text{F}$, ${}^{19}\text{-}27\text{Ne}$, ${}^{21}\text{-}29\text{Na}$, ${}^{23}\text{-}31\text{Mg}$, ${}^{24}\text{-}34\text{Al}$, ${}^{26}\text{-}34\text{Si}$, ${}^{29}\text{-}36\text{P}$, ${}^{30}\text{-}37\text{S}$, ${}^{33}\text{-}37\text{Cl}$, ${}^{35}\text{-}39\text{Ar}$, and ${}^{37}\text{-}40\text{K}$. The potassium isotopes should be produced by the reaction with proton pick-up process.

In order to obtain the doubly-differential cross section from each fragment yield, we estimated the transmission between F0 to F2, and the reaction loss in the detectors. A Monte Carlo simulation by MOCADI [2] was performed under the realistic condition of RIPS using a reference beam of ${}^{40}\text{Ar}$. The value of transmission was obtained to be $95.3 \pm 0.3\%$. The nuclear reaction loss of fragment in the detectors was evaluated with reaction cross sections calculated by a simple geometrical model. The reaction loss in the detectors was estimated to be less than 0.8%. After all, the systematic error was $\pm 9\%$ for evaluation of the fragment cross sections.

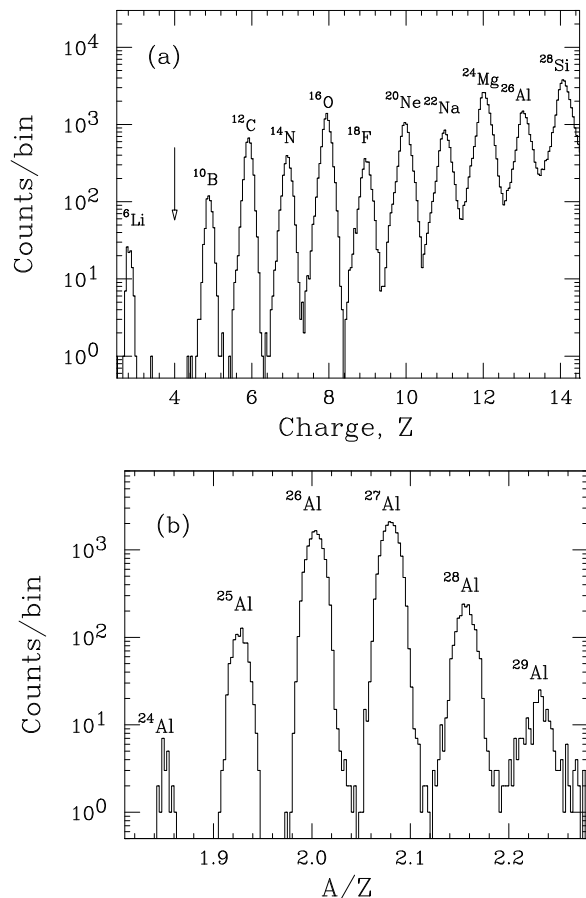


FIG. 2: (a) Z-projection spectrum for $A/Z=2\pm 0.3$ and (b) A/Z-projection spectrum for $Z=13.0\pm 0.5$ at $B\rho=2.523$ Tm (Be target). The arrow in (a) indicates the lack of ^8Be , which is known to be particle unbound.

B. Fitting Procedure

Momentum distributions of fragments have information for understanding reaction mechanisms. At relativistic energies, the projectile fragments have symmetric momentum distributions fitted to a Gaussian form, of which width has been discussed with respect to the Fermi motion of nucleons or temperatures of pre-fragments [12].

The results obtained in this work are different from at relativistic energies. Figure 3 shows a typical momentum distribution of this experiment. By comparison of the momentum distribution fitted with a Gaussian function (dotted curve), asymmetric feature of the distribution is clearly observed. The momentum distribution of projectile-like fragments produced at intermediate energies are generally asymmetric with a tail on the low momentum side [17].

To deduce the most probable momentum and width from such skewed shapes, the momentum distributions have been fitted so far with several kinds of trial functions [17, 18, 19]. Since physical models have not been established for the low momentum tail, what kind of func-

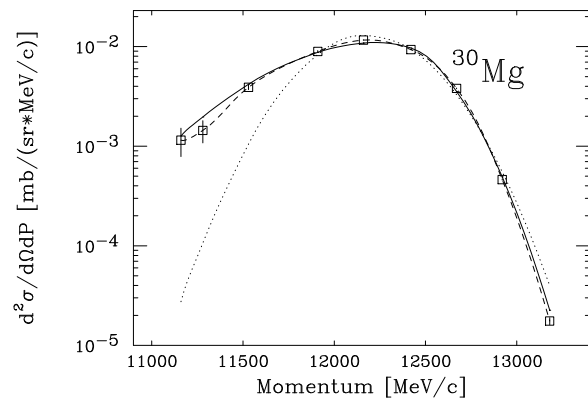


FIG. 3: Typical fragment momentum distribution (dashed curve) and fitting results for the momentum distribution of ^{30}Mg data. The fitting result with a Gaussian function (dotted curve) shows clearly asymmetric feature of the experimental data. The solid curve indicates a fitting result with the asymmetric Gaussian function.

tions to be used is not unique. To study a systematics of low-momentum tail, the following asymmetric function with four free parameters is applied for the present data fitting,

$$\frac{d^2\sigma}{dP d\Omega}(\theta = 0^\circ) = \begin{cases} A \cdot \exp\left(-\frac{(P - P_0)^2}{2\sigma_L^2}\right), & P \leq P_0 \\ A \cdot \exp\left(-\frac{(P - P_0)^2}{2\sigma_H^2}\right), & P \geq P_0 \end{cases}, \quad (4)$$

where P_0 is the most probable peak value of momentum in the distribution, σ_L and σ_H are momentum width in low and high energy side, respectively.

In this fitting procedure, the maximum likelihood method was used to treat the small statistics at the tail parts of distribution. The result of fitting with the asymmetric Gaussian function is shown with the solid curve in Fig. 3.

By means of this method, we obtained fitting results of momentum distribution for all isotopes available in our data, though there is another kind of complexity in a few case. We found two components in the momentum distributions of very light fragments only for the Be-target data. Figure 4 shows the momentum distributions of the ^{10}Be and ^{30}Mg isotopes from the Be-target data. The both distributions are scaled as a function of velocity (β). Two arrows in the figure indicate the velocities of projectile (β_{proj}) and center-of-mass system (β_{cm}), respectively. In the distribution of ^{30}Mg (Fig. 4(b)), a single component is observed near the projectile velocity (β_{proj}). On the other hand, the ^{10}Be distribution (Fig. 4(a)) shows two components at β_{proj} and β_{cm} . Here, the component around β_{proj} is defined as a high-energy side of peak (HE), and that of β_{cm} is as a low-energy side of peak (LE). We made an attempt to fit the data using the asymmetric Gaussian function for the HE-component and a Gaussian function for the

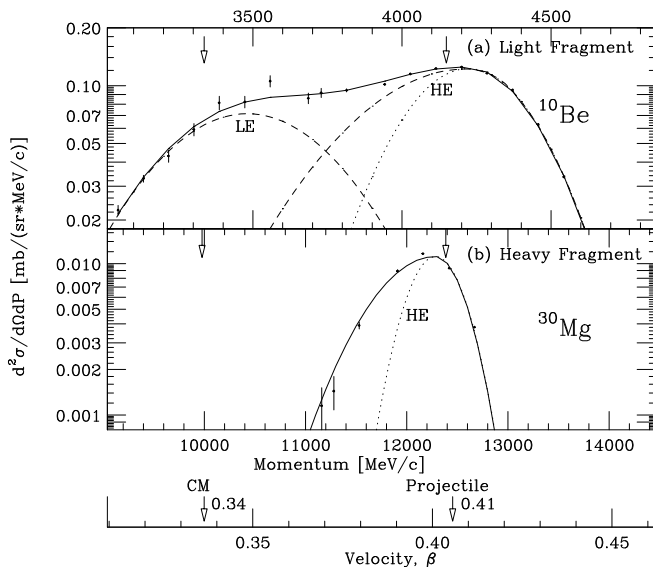


FIG. 4: Typical fragment momentum distributions for (a) ^{10}Be and (b) ^{30}Mg produced in Ar+Be reaction. The fitting results are also shown with solid curves. Light fragment of ^{10}Be has two components (dashed curves) of HE- and LE-components, while heavy fragment of ^{30}Mg has one component corresponding to HE-component. The HE-component for each isotope has a low momentum tail and the symmetric parts are shown with dotted curves.

LE-component. The fitting results are drawn with solid curves. With increasing the fragment mass number, the LE-component decreases very quickly. At last, no significant LE-component has been observed for heavy fragments like the ^{30}Mg data. In our data, we have found clearly the LE-component for the fragments with A of 9~12. The LE-component has been observed for light fragments in Ar+Be reaction, while, the LE-component has not been found in the momentum distributions of Ar+Ta reaction data in the momentum region where the experimental data were taken. When a light fragment like ^{10}B is produced in the Ar+Ta reaction, the impact parameter is much larger than in the case of the Ar+Be reaction. Thus, we found the LE-component only for the Ar+Be system. Since we focus on the projectile fragmentation reaction, we discuss mainly the HE-component in this paper.

C. Evaluation of cross sections

The production cross sections of fragments were evaluated with the fitting results of the longitudinal momentum distributions. The transverse momentum distributions are assumed to be a Gaussian function with a width of σ_{\perp} ,

$$\sigma_{\perp}^2 = \sigma_H^2 + \frac{A_f(A_f - 1)}{A_p(A_p - 1)} \sigma_D^2, \quad (5)$$

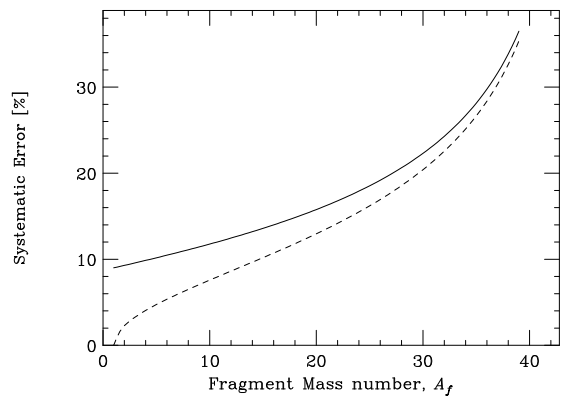


FIG. 5: Overall systematic error for the production cross sections (solid line). The dashed line shows error originated from ambiguity of σ_{\perp} .

where σ_D is a parameter of the deflection effect, and $A_{p,f}$ are mass numbers of a projectile and a fragment, respectively. In Ref. [20], the deflection parameters for two targets of ^{27}Al and ^{197}Au with 92.5 and 117.5 A MeV ^{16}O beams. The results from their measurement were $\sigma_D = 190\text{--}220$ MeV/c, found no large target dependence. Taking account of an energy dependence reported in Ref. [21], we used σ_D of 195 MeV/c around 90 A MeV for the present experiment. The ambiguity of transverse momentum distributions was taken into account as the systematic error of the cross sections. The overall systematic error for the production cross sections is shown in Fig. 5.

IV. RESULTS AND DISCUSSION

The fitting results with the asymmetric Gaussian function are presented in the following. First of all, the fitting results of momentum distributions are compared with several formulae taken from reaction models. The result of high momentum side width can be understood by the Goldhaber model. However, we need the further discussion of the momentum peak shift and low momentum side width. Next, we show the result of production cross sections. The result reveals the phenomena, breakdown of factorization (BOF), for production of very neutron-rich nuclei. We discuss the systematics of isotope production cross sections. The charge distribution of the cross sections for a fragment mass is obtained from our data, and compared with the EPAX formula. Finally, we discuss the prefragment production mechanism in projectile fragmentation reactions to search for the origin of BOF.

A. Momentum peak shift

In the nuclear fragmentation process, a part of the kinetic energy of projectile is converted into excitation

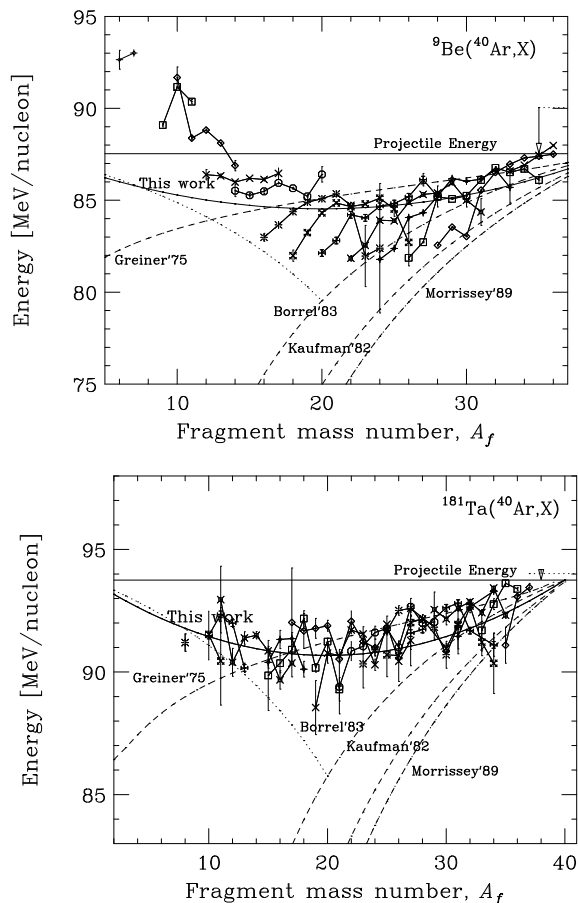


FIG. 6: Momentum peak shift of fragments produced in (upper) Ar+Be and (lower) Ar+Ta. The primary beam energies are drawn with dotted lines, and the kinetic energies at the half point of target thickness (projectile energies) are the solid lines. See the text for the labels and curves.

energies of fragments, and the projectile velocity is decreased. This energy loss in projectile fragmentation reaction is called as ‘momentum peak shift’. The momentum peak shift is obtained from the difference of the projectile velocity and the most probable velocities of fragments. We present the result of momentum peak shift in a unit of energy per nucleon, which is proportional to square of velocity. This unit is convenient to discuss the kinetic energy consumption in the nuclear reaction.

Figure 6 shows the momentum peak shift of fragments produced in Ar+Be and Ar+Ta reactions. The solid lines for each isotope are drawn to guide the eye. The primary beam energies were corrected with the mean energy loss in the production target. The obtained projectile energies (solid lines) were taken to be 87.5A MeV and 93.8A MeV, respectively. The values of the most probable energies of fragments were also corrected with energy losses in the targets. The negative shift of data from the solid line of the projectile energy indicates the energy loss by nuclear fragmentation process. The systematic error of momentum shift was estimated to be 0.9% in the unit of

energy per nucleon.

The deviation for a given element chain in the Be target is comparable to the systematic error. As seen in Fig. 6, the measured momentum shifts for the Be target (a), compared with the case of the Ta target (b), vary widely. One could understand the deviation as an effect of the target thickness in atomic energy-loss process [22], because the target thickness of Be is six times thicker than that of Ta.

The bounce of momentum peak shift as a function of fragment mass was observed in the results of both targets. The momentum peak shift increases when the number of removed nucleons $\Delta A = A_p - A_f$ is increased up to a half of projectile mass ($A_f \geq 20$). On the other hand, the momentum shift decreases when the mass loss ΔA is increased beyond 20 ($A_f < 20$). In short, we observed the maximum of momentum peak shift around $A_f = 20$.

A phenomenon of fragment acceleration was observed in the Be-target data. In Fig. 6(a), the solid line of 87.5A MeV corresponds to the primary beam energy. Velocities of the fragments ${}^6,7\text{Li}$, ${}^9-11\text{Be}$, and ${}^{10-13}\text{B}$ are larger than the projectile velocity. The very light fragments are accelerated in the reaction process. We note that the acceleration phenomena was also observed in collisions of ${}^{238}\text{U}$ at 1 A GeV with lead, reported by Enqvist [23]. On the other hand, no acceleration phenomenon for all fragments $A_f \geq 8$ was observed in the Ta-target data.

Except the acceleration phenomenon, no significant difference between both targets was observed in the momentum peak shift for the projectile-like fragments $A_f \geq 20$.

We found two features in the momentum peak shift. First, the maximum of momentum peak shift is observed for the fragments around $A_f = 20$ in Fig. 6 for both targets. Secondly, the acceleration phenomenon was observed in light fragments only for the Be target. Namely, the most probable velocities of light fragments are beyond the projectile velocity. In the following, we discuss the features observed in the momentum peak shift.

1. Parabolic mass dependence of peak shift

The momentum peak shift has been investigated for long time. Many of the reports have shown a linear mass dependence of the peak shift for fragments with $A_f \geq A_p/2$. Several formulae are proposed so far to reproduce the momentum peak shift for the heavy fragments produced in peripheral collisions. We compare our experimental results for the wide fragment mass range with the formulae and make an attempt to introduce a new picture to reproduce the parabolic mass dependence.

In Fig. 6, four formulae are shown with dashed curves and the labels as Greiner75, Kaufman82, Borrel85 and Morrissey89 [24, 25, 26, 27, 28, 29, 30]. For every formula, the momentum shift becomes large when the number of removed nucleons ΔA is increased up. This tendency conflicts the present result in the region of $A_f \leq 20$.

To compensate for the deviation, J.A.Winger et al. [1] obtained a formula symmetrized mathematically with respect to $A_p/2$ (dotted line). However, it still overestimates the momentum shift around $A_f \sim A_p/2$. After all, all of formulae above cannot predict the parabolic mass dependence.

The previous investigations were mainly performed in the region of fragments close to the projectile mass. For whole fragment mass region observed in this work, a parabolic dependence, where the symmetric point is at the half mass of projectile, is observed. As Borrel commented first in Ref. [30], the symmetric behavior of the velocity shift implies another mechanism less costly, compared with the removal of individual nucleons. The mechanism may be a process that the projectile splits into two pieces. Then we make a new formula which calculates the momentum shift based on the splitting picture.

First, we assumed that the projectile splits in two fragments which are not excited state. By means of the empirical mass formula of Weizsäcker-Bethe $M(N,Z)$, where (N,Z) is the neutron and charge number of nuclei [31], the energy loss in the splitting process is described as $M(N_f, Z_f) + M(N_p - N_f, Z_p - Z_f) - M(N_p, Z_p)$. The change of binding energy shows the parabolic mass dependence of peak shift. However, the energy loss by the splitting process gives only several tens percent of the value measured as momentum peak shift, quantitatively.

Next, we deduce a semi-empirical formula in consideration of the excitation energy of fragments. The splitting process consumes the kinetic energy of projectile due to the excitation. Here we assume that the energy consumption is proportional to the number of pairs of nucleons destroyed in the reaction, where the nucleons are acting mutually by long range force. In this picture, the number of pairs of nucleons in projectile is counted with $A_p C_2 = A_p(A_p - 1)/2$, where the mark of ${}_n C_m$ is the combinatorial which gives the number of ways of choosing m out of n . When the projectile splits into the spectator A_f and the participant $(A_p - A_f)$, the number of pairs of nucleons which decreased by reaction serves as $A_f(A_p - A_f)$. When one nucleon is removed ($A_f = A_p - 1$), the number of pairs which decreased is $A_p - 1$, and the total energy loss can be defined as ε MeV. The energy loss per a nucleon pair is $\varepsilon/(A_p - 1)$ MeV on average. Thus, the kinetic-energy loss in the splitting process can be written as,

$$\Delta E = \frac{\varepsilon A_f (A_p - A_f)}{A_p - 1}. \quad (6)$$

In the case of non-relativistic beam energy, the energy conservation between projectile and two pieces gives a new formula as follows:

$$\frac{v_f}{v_p} = \sqrt{1 - \frac{\varepsilon A_f (A_p - A_f)}{A_p E_p (A_p - 1)}}. \quad (7)$$

If we select the energy loss parameter of $\varepsilon = 8$ MeV, this formula corresponds to Borrel's for the case of one-nucleon removal. However, the value of ε may not be

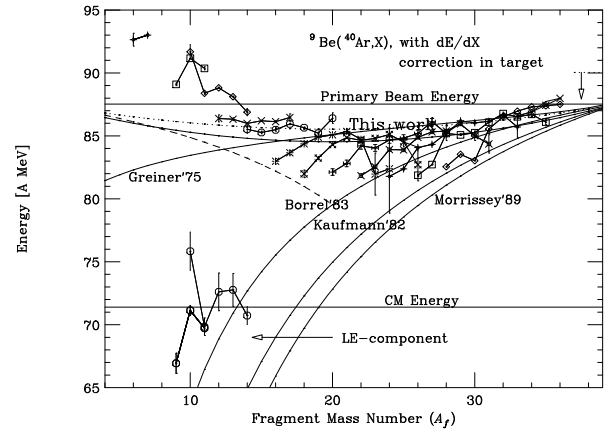


FIG. 7: Peak value, P_0 , of fragment momentum distribution for HE-component and LE-component.

8 MeV. In Fig. 6, the P_0 values predicted by the formula were compared with the present data. The solid curve (this work) was drawn with $\varepsilon = 12$ MeV to fit the data. The experimental data may support that $\varepsilon = 12$ MeV is better than 8 MeV.

2. Acceleration phenomenon

The acceleration effect cannot be explained by a fragmentation model based on the abrasion-ablation picture, in which the projectile always loses the kinetic energy in the laboratory system for abrasion process of nucleons.

The acceleration phenomenon may be peculiar to the ${}^9\text{Be}({}^{40}\text{Ar}, X)$ reaction, namely inverse kinematics. No acceleration effect was found in the Ta target data. By comparison between both targets, we found two particular features of momentum distributions for light fragments produced in the Ar+Be reaction. One feature is the acceleration phenomenon. The other feature is the existence of LE-component. Both phenomena coincide in our data. Therefore, the acceleration phenomenon may be related to the LE-component.

F. Auger et al. [32] have suggested that the light fragments originate in division of a composite system. In their experiment of ${}^{86}\text{Kr} + \text{C}$ and ${}^{86}\text{Kr} + \text{Al}$ collisions, the energy of the Kr beam was $35A$ MeV, and relatively lower than our experiment. As a result of their experiment, two components of fission-like fragments were found in the velocity distribution of fragments with each mass number. The two components may be generated from a highly excited compound system since the average speed of them was equal to the center-of-mass (CM) speed of the incident system. In short, it is possible that the LE-component and the HE-component come from one source.

As shown in Fig. 7, the velocities of the LE-component observed in this work are not below but just on the CM velocity. In addition, the mean energy of HE- and LE-

component is around $80A$ MeV. Thus, the observed phenomenon is different from the work of F. Auger et al.

Then, we suggest two source model that the LE-component and the accelerated HE-component come from two sources produced in different reactions, respectively. One source is an excited compound system from projectile and target nuclei running on the CM velocity. The source emits light particles homogeneously in angular space and becomes a fragment in the LE-component. On the other hand, the other source is a hot projectile. The hot projectile is formed by a strong impact of target nucleus to convert the kinetic energy of projectile nucleus to the internal energy for the excitation of projectile nucleus. The hot projectile decays to two components again, which consists of a faster component and a slower component than the projectile velocity, like the one-source model. This two-source model predicts a third component in the momentum distribution of light fragments. Such third component was not observed in our data. After all, the origin of the acceleration phenomenon has not been understood so far.

Neither the acceleration effect nor the LE-component were found in the Ta target data. The different situation from the Be target comes from the large impact parameter. For a fragment mass, the impact parameter in the Ar+Ta reaction is larger than in the Ar+Be reaction when the fragment is formed by the geometrical cut. The hot compound system is not produced in the peripheral collision with the large impact parameter. Therefore, the exotic phenomena may not be observed in the Ta target data.

B. High momentum side width

The high momentum side widths σ_H as a function of fragment mass are shown in Fig. 8(a) and Fig. 9(a), for the Be and Ta targets, respectively. The high momentum side widths of all the observed fragments are compared to the formulation by Goldhaber as follows,

$$\sigma_{||} = \sigma_0 \sqrt{\frac{A_f(A_p - A_f)}{A_p - 1}} \quad (8)$$

where $A_{p,f}$ is the mass number of the projectile and fragment, respectively. The solid curves are drawn with the reduced width $\sigma_0=90$ MeV/c from experimental results at relativistic energies [12]. The deduced values of σ_0 for the fragments in the mass range 9 to 36 are shown in Fig. 8(b) and Fig. 9(b). The dashed lines denote the mean value of $\sigma_0 = 93.5 \pm 2.6_{stat} \pm 7.5_{sys}$ MeV/c for the Be target, and $97.4 \pm 1.8_{stat} \pm 7.8_{sys}$ MeV/c for the Ta target, respectively. No significant difference between both targets was observed in the high momentum side widths. The light fragments $A_f < 13$ produced by using the Be target show slightly a deviation from the Goldhaber model. The deviation is originating from the LE-component and the fitting function to be used. To avoid a digression from the

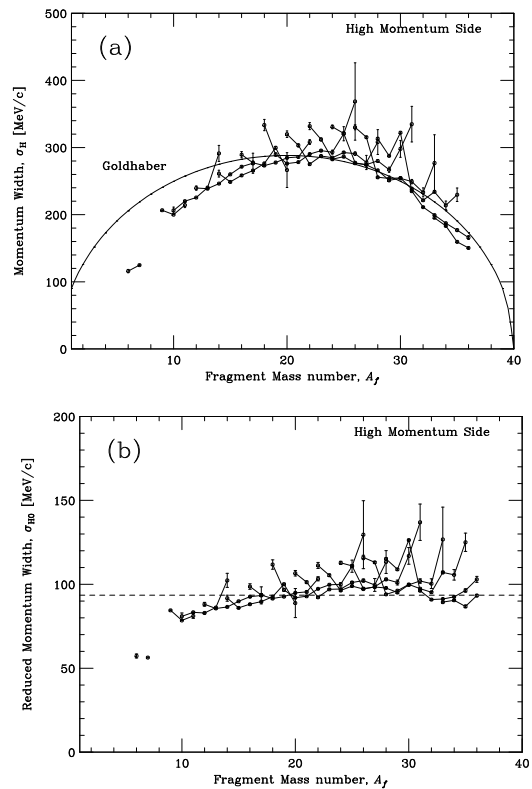


FIG. 8: Momentum widths at high momentum side (Be target); (a) for σ_H and (b) for reduced widths according to the Goldhaber model.

main purpose, we do not follow up the deviation further. These results are in good agreement with high-energy experiments [12].

At relativistic energies, the reduced width σ_0 is independent of the primary beam energy. At lower energies, the reduction of σ_0 has been observed [33]. The reduction mechanism has been argued by several theoretical works, where the reason is for example due to the Pauli blocking. Due to the effect, the σ_0 has the energy dependence at 30-40A MeV [29, 34], and becomes constant up to 90A MeV. The fact that the measured σ_0 is the same as high-energy one is consistent with this picture.

C. Low momentum side width

The results of momentum width at low momentum side are shown in Fig. 10. The widths of low momentum side σ_L are plotted as a function of fragment mass with the statistical errors. We compared the results with the high momentum side width σ_H . Instead of showing individual data of σ_H , the dashed curve calculated with the Goldhaber model is presented. The systematic error of σ_L is estimated to be 8%, which is not shown in the figure.

In the Be-target data, each isotope chain has a mountain-style structure (solid curves). On the other

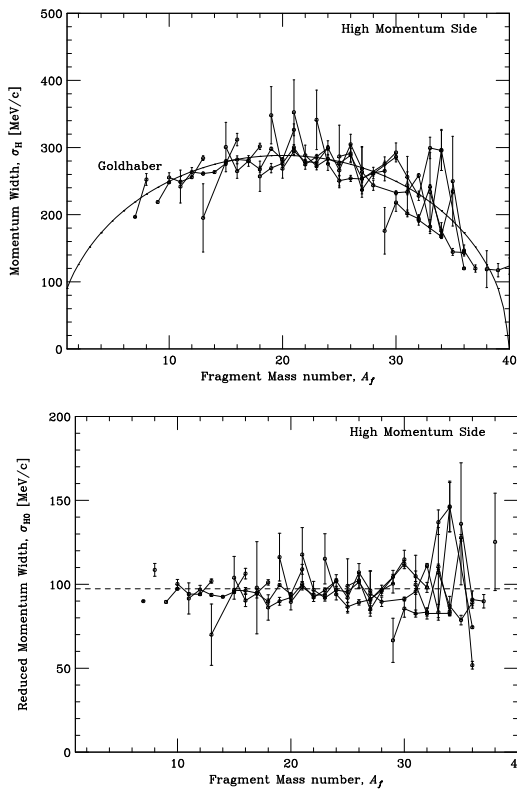


FIG. 9: Momentum widths at high momentum side (Ta target); (a) for σ_H and (b) for reduced widths according to the Goldhaber model.

hand, the low momentum widths σ_L of the Ta data may have no such a structure. One can understand the deviation as the target thickness effect. Another reason for the mountain-style structure should be noted. The momentum distribution of light fragments has the LE-component at the low momentum side only for the ^9Be target data. In the fitting procedure by use of the asymmetric Gaussian-like function, the LE-component may also affect the results. Therefore, the mountain-style structure of σ_L for fragment mass should be ignored as a systematic error.

As seen in Fig. 10, the measured widths of σ_L are twice wider than σ_H approximately. Obviously, the large width cannot be explained by the Goldhaber model. The σ_L may have a linear dependence as a function of mass loss $\Delta A = A_p - A_f$, which is very different from the parabolic feature of σ_H . No target dependence of σ_L between the Be and Ta targets was found in our data. As any models for the low momentum tail have not been established, it is difficult to discuss the low momentum tail only from the systematics of σ_L . Yet we should comment that the low momentum tail may not depend on the target.

In addition, another interesting point was found in the result. At the limit $\Delta A \rightarrow 0$, the σ_L may not converge on 0, but 300~400 MeV/c. This feature is different from the Goldhaber formula. Even if the fragmentation reaction is the dominant process for production of fragments, these

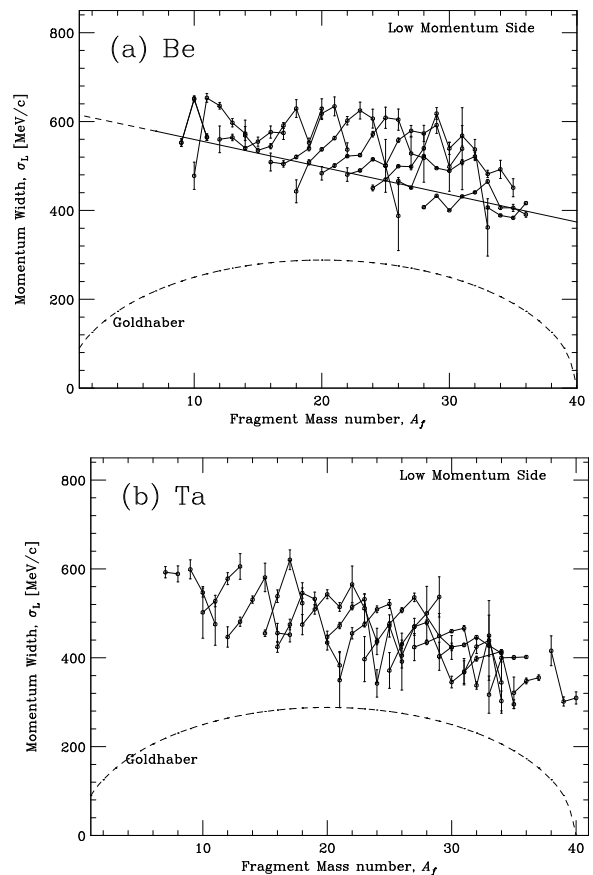


FIG. 10: Momentum widths at low momentum side by using (a) the Be target and (b) the Ta target. The solid lines in both figures are the linear fitting of the Ta target data. The experimental results (σ_L) and the fitting lines are located far from a prediction of the Goldhaber model. The isotope chains of experimental data are also drawn as solid lines.

new observations may lead to an additional reaction process necessary for intermediate-energy reactions.

In Fig. 10, a fitting line was first obtained from the Ta data. The fitting lines are drawn in both figures. The experimental results (σ_L) and the fitting lines are located far from a prediction of the Goldhaber model.

What is the origin of the large width of low momentum side? The large width is indeed produced by an energy-loss process in the nuclear reaction. The energy-loss process for σ_L may be different from the “pure” fragmentation process, because the width of low momentum side strongly depends on the beam energy. At relativistic energies, the momentum distribution becomes symmetric with $\sigma_L = \sigma_H$. For a low energy beam at 30A MeV, the large tail of low momentum side appears obviously [35]. Macroscopic friction process of nuclear dissipation is not the satisfactory mechanism for σ_L because the momentum peak P_0 , which has no significant energy dependence, may also be changed at the same time.

The energy-loss process to produce the width of low momentum side may be explained by nucleon exchange

reaction between target and projectile [36]. For instance, transfer mechanism adds one nucleon to the projectile or fragment, the energy per nucleon E may be changed as $E_{+1n} = E \cdot A/(A+1)$, where A is the mass number before transfer reaction. Since the velocity of projectile is reduced by the nucleon exchange reaction, the nucleon transfer may contribute the low momentum tail. When the projectile gives a nucleon to the target nuclei, the velocity of the remained nucleons in the projectile does not change significantly. Like the effect of momentum peak shift, the change of potential energy in projectile affects slightly the velocity of projectile nucleus. On the other hand, when the projectile picks up a nucleon from the target nuclei, the projectile velocity should be deduced because nucleons in target nuclei are much slow on average at the laboratory system. Thus, we suppose the nucleon exchange reaction as an origin of the low momentum tail.

Assumed that the probability of nucleon exchange is described as the Poisson distribution and the average of number of transfer nucleons in a reaction is quite small, the transfer process does not contribute the peak shift of fragment-momentum distribution but the large width of low momentum tail. If the probability of transfer process is small on average, the peak shift of fragment-momentum distribution, which is related to the case of no nucleon transfer, does not suffer from the transfer process to be independent of the beam energy. On the other hand, the low momentum width is sensitive to the transfer probability.

We next discuss the linear dependence of σ_L as a function of ΔA . First, we try to explain this dependence in terms of the surface abraded. If the transfer probability is proportional to area of the surface, the probability may be described as a symmetric function with respect to the half of projectile mass. However, the observed behavior has a linear dependence. So, the abraded surface may not be directly related to the transfer process.

Secondly, we think about the overlap volume of projectile and target nuclei, i.e., total number of nucleons in the participant region. The region has almost linear dependence as a function of A_f . Thus, the linear dependence of σ_L may be related to the volume of the overlap region.

D. Transfer-like fragmentation

The transfer-like fragments of ^{36}Al , $^{37,38}\text{Si}$, $^{38,39}\text{P}$, and $^{37-40}\text{K}$ were observed at this experiment. These fragments have more neutrons or protons than the projectile nucleus. The fragments cannot be produced with projectile fragmentation reactions. Neutron and proton pick-up processes are necessary for production of the fragments.

Figure 11 shows the momentum distribution of ^{36}Al acquired by using the Be target. This isotope production needs at least one neutron pick-up process from target nucleus. We made an attempt to fit the momen-

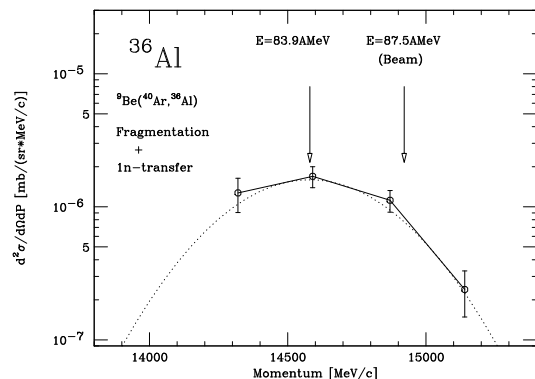


FIG. 11: Momentum distribution for ^{36}Al . This isotope cannot be produced with only the nuclear fragmentation process. One neutron should be picked up from target. The measured peak momentum corresponds to 83.9A MeV. The measured momentum peak shows a larger shift toward low momentum side, compared with that of the same mass number, $\sim 0.9A$ MeV.

tum distribution with the asymmetric Gaussian function. Due to the lack of data at low-momentum tail, we assumed that the fitting parameters of momentum widths were fixed. The σ_H was given from the Goldhaber formula with $\sigma_0=90$ MeV/c. The σ_L was assumed to be $(400 \pm 60_{sys})$ MeV/c. This value was obtained from the systematics as shown in Fig. 10.

The fitting result is shown as a dotted curve in Fig. 11. The peak of the momentum distribution corresponds to 83.9A MeV. As the primary beam energy was measured as 87.5A MeV, the momentum peak shift was obtained as (3.6 ± 1.2) A MeV.

The measured momentum peak shows clearly a larger shift toward low momentum side, compared with that of the same mass number, $\sim 0.9A$ MeV. The large momentum shift of transfer-like fragments was also observed in the fragments of $^{37-40}\text{K}$ requiring to proton pick-up process in production.

E. Target dependence of cross sections

The target dependence of cross sections was investigated with the results of our experiments. We have obtained the cross sections in wide range of fragment charge for each fragment mass with small statistical and systematic errors, and for the same projectile (^{40}Ar) with two sets of targets (^9Be and ^{181}Ta). So we can investigate the validity of factorization for fragmentation reactions at intermediate energies.

Figure 12 shows the ratios of cross sections for a fragment in Ar+Ta reactions to those in Ar+Be reactions. The cross sections are normalized with the experimental mass yield $Y(A_f)$ to eliminate the target size effect. The mass yields were obtained from the sum of fragment cross sections with the same mass number. The ratio is shown as a function of charge difference between the

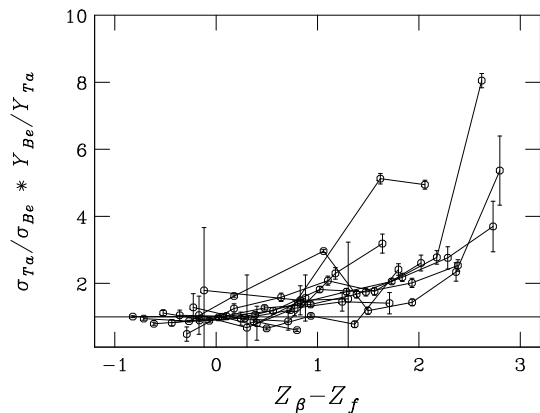


FIG. 12: Ratio of the production cross sections for each fragment produced with Be and Ta targets. The solid lines are drawn for the same mass number of nuclei, i.e. isobars. The Z_{β} is the β -stable charge for each isobar. The cross-section ratio of $\sigma_{Ta}(A,Z)/\sigma_{Be}(A,Z)$ is normalized with the mass-yield ratio of $Y_{Ta}(A)/Y_{Be}(A)$ observed.

most stable charge $Z_{\beta}(A_f)$ and the fragment charge Z_f . Thus, the target dependence of projectile fragmentation cross sections except the target size effect is represented for the wide range of isotopes near and far from the stability line. If the factorization is valid for production of an isotope, the ratio has no $Z_{\beta} - Z_f$ dependence.

In Fig. 12, the ratios near the β -stability line are constant. It corresponds that the factorization is valid for the production of the nuclei. According to the previous work [37], the factorization is valid for the isotopes in $Z_{\beta} - Z_f \leq 2$. On the other hand, the ratios increase when $Z_{\beta} - Z_f$ is increased. This deviation shows that the factorization hypothesis is clearly broken down for neutron-rich nuclei with $(Z_{\beta} - Z_f) \geq 2$.

F. EPAX formula

The EPAX was developed by using data of the spallation reactions and heavy-ion induced fragmentation reactions at several A GeV [38]. The cross section of a fragment with mass A and proton number Z produced by projectile fragmentation from a beam (A_p, Z_p) impinging on a target (A_t, Z_t) can be written as,

$$\sigma(A, Z) = Y(A) \cdot W(A, Z) \quad (9)$$

$$W(A, Z) = n \cdot \exp(-R \cdot |Z_{prob} - Z|^U) \quad (10)$$

where $Y(A)$ represents the mass yield which is the sum of the isobaric cross sections for fragments with mass number A , and $W(A, Z)$ describes the charge distribution which means the cross-section distribution of a given fragment mass which has a maximum peak at Z_{prob} .

The charge dispersion $W(A, Z)$ is described as R , Z_{prob} and U parameter. The most probable charge, Z_{prob} , is

written as,

$$Z_{prob} = Z_{\beta} + \Delta + \Delta_m, \quad (11)$$

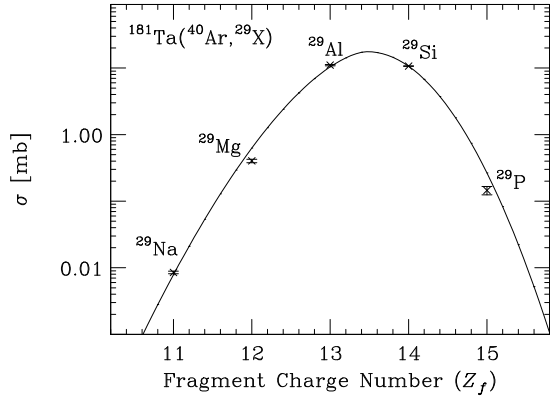
where Z_{β} is the β -stable charge for a fragment of mass number, A [39], Δ is a proton-excess between the stability line and the most probable line of fragmentation reaction, and Δ_m is the so-called ‘‘memory effect’’, i.e., the influence of the projectile N/Z ratio on the fragment N/Z ratio. The R is a function of fragment mass number, A , which shows a fragment mass dependence of a steepness controlling cross sections of isotopes from the stability line to the drip lines. The mass dependence has been confirmed from many combinations of projectiles and targets. The U parameter is given as a constant for all neutron-rich isotopes so far.

Using new data obtained mainly at the GSI/FRS facility, the EPAX was recently modified [3] slightly to tune the mass yield and the U parameter for proton-rich fragments in the vicinity of projectiles. The present paper focus on the neutron-rich fragments in a wide range. Thus, this work gives the analysis and discussion using the EPAX formula based on the original EPAX that has relatively simple functions.

The EPAX formula is valid for the ‘‘limiting fragmentation’’ regime, where the fragmentation process is no longer energy dependent. The energy dependence of fragmentation cross sections has been investigated by Silberberg and Tsao [40, 41]. We can see the similar energy dependence in the total reaction cross section. The total reaction cross section has been studied both theoretically and experimentally for more than 50 years. A detailed list of reference is found in Ref. [42]. Compare the cross section of $^{12}\text{C}+^{12}\text{C}$ at 90A MeV with 900A MeV, the difference of cross sections is about 30% [43]. This value is nearly equal to the systematic error of measured cross sections in this work. Thus, we can assume that the limiting fragmentation hypothesis is valid in this work.

The EPAX formula follows the factorization hypothesis. The mass yield has a target dependence, however it is limited to the target nuclear-size effect. The charge dispersion $W(A, Z)$ is independent of the target nucleus.

In this work, however, the BOF has been found in the production of very neutron-rich nuclei. An investigation of the charge distribution is necessary to find appropriate description for cross sections from our data. In the charge distribution of EPAX, the U parameter is a constant of 1.65 for neutron-rich side, and has no target dependence. The value of U parameter is very sensitive to the production cross sections of the isotopes far from the β -stability line. In the following, we reduce the U parameter for each fragment mass with both targets from our data. At the same time, we investigate the target dependence of Z_{prob} since Z_{prob} is also sensitive to the cross sections of isotopes far from the β -stability line.

FIG. 13: Charge distribution for $A_f=29$.

1. Charge distribution

A fitting of the production cross sections was performed using the EPAX function. The function is represented as the product of $Y(A)$ and $W(A, Z)$. The charge distribution $W(A, Z)$ is characterized with the most probable charge Z_{prob} , the slope constant U and the width parameter R . The R parameter has slightly fragment-mass dependence and an effect to the slope of charge distribution. We have two kinds of U parameters of U_p for proton-rich side and U_n for neutron-rich side. In the fitting procedure, the values of the U_p and the R parameters are fixed, originally given by the EPAX formula. The fitting procedure was performed with the experimental data of each fragment mass. First, we obtain the maxima of the charge distribution $Z_{prob}(EXP)$ as a function of fragment mass number from the experimental data with both targets. The values are compared with the EPAX ones, the β -stability line, and N/Z ratio of projectile nuclei. Next, the U parameters are deduced from the data when we assume the same parametrization of Z_{prob} for both of the targets.

We have investigated the target dependence of Z_{prob} . The measured cross sections for each fragment mass were fitted with $Y(A) \times W(A, Z)$. The mass yield Y is a constant for a fragment mass. Fitting parameters were U parameter in neutron-rich side, Z_{prob} , and the mass yield. Figure 13 shows the charge distribution of fragment mass 29, produced in Ar+Ta reaction. The Z_{prob} is obtained as $13.47 \pm 0.01(stat) \pm 0.04(sys)$. Similarly, the Z_{prob} value for each fragment mass is deduced from our experimental data.

The experimental Z_{prob} is compared with the value from the EPAX formula. Figure 14 shows the deviation of $Z_{prob}(EXP)$ from $Z_{prob}(EPAX)$ for Ar+Be and Ar+Ta data. Solid lines are drawn to guide the eye. The EPAX reproduces the Z_{prob} very well, especially for the mass number between 20 to 35. The deviation of Z_{prob} is less than 0.2. Due to the lack of proton-rich side data, we obtained only three values of Z_{prob} for the Ar+Be data in $A_f=18, 22$ and 26 . To compare both data of Be and Ta

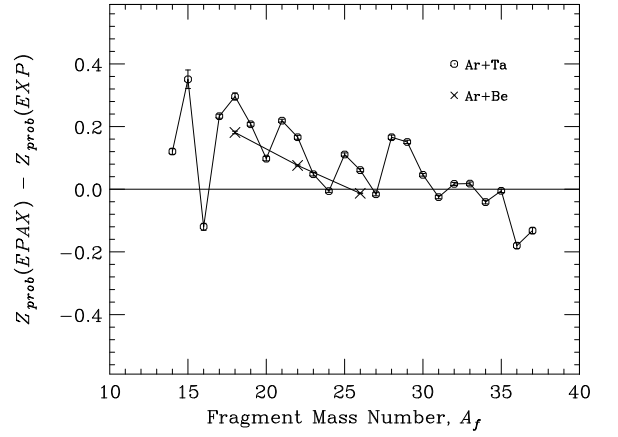
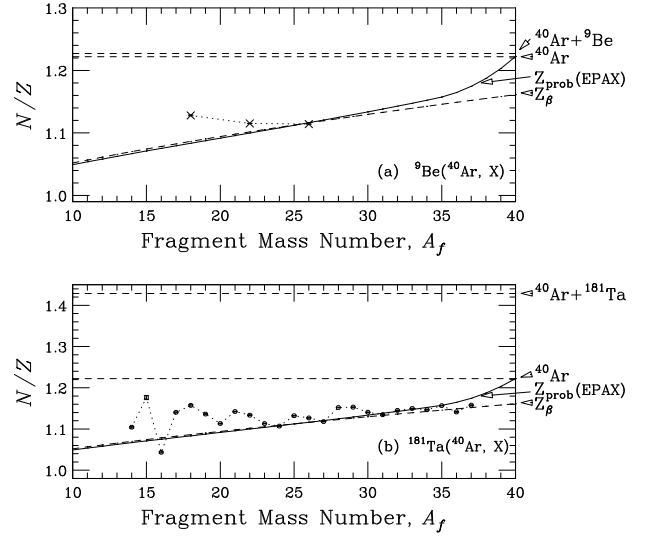


FIG. 14: Deviation of the most probable charge from the EPAX parametrization to experimental data for the production targets of Be and Ta.

FIG. 15: Peak of charge distributions as a function of fragment mass for the production targets of (a) Be and (b) Ta. The solid curves are the most probable charge Z_{prob} of EPAX. The dashed curves are the β -stable charge Z_β . The dashed lines are the N/Z ratio of ^{40}Ar projectile and compounds of $^{40}\text{Ar}+^9\text{Be}$ and $^{40}\text{Ar}+^{181}\text{Ta}$, respectively.

targets shows no significant target dependence of Z_{prob} .

Figure 15 shows the most probable charge in N/Z unit as a function of fragment mass for the Be and Ta targets. The most probable charge Z_{prob} from the EPAX is close to the β -stable charge Z_β . The ratio N_p/Z_p of the projectile is 1.22. For the composite system of projectile and target, the ratio is represented as $(N_p + N_t)/(Z_p + Z_t)$, of which values are 1.23 and 1.43 for Ar+Be and Ar+Ta, respectively. The $Z_{prob}(EXP)$ is well described as the $Z_{prob}(EPAX)$ as well as Z_β . The difference of $Z_{prob}(EPAX)$ and Z_β is mainly the memory effect Δ_m . The memory effect is not clearly seen in our data.

No significant difference of $Z_{prob}(\text{EXP})$ between the Be and Ta targets has been observed, however the BOF has been found in the very neutron-rich nuclei. What does it mean? It should be noted that the BOF had never been found in the projectile fragmentation at other experiments. This fact is consistent with our observation of $Z_{prob}(\text{EXP})$ for the Be and Ta targets. To understand the charge distribution, we show the Z_{prob} of projectile-like fragments produced by the reactions at low and intermediate energies.

At low energies, the most probable charge shows the existence of two different reaction mechanisms. In Ref. [44], Cl isotopes were produced in 7.4-MeV $^{40}\text{Ar}+^{50}\text{Ni}$ reaction and the contour plots of the Cl isotope yield were drawn to the fragment mass and the kinetic energy. We clearly see two components, one corresponding to quasi elastic reactions centered at a high energy and a mass of 39. The second one is centered around a mass of 36 and a small kinetic energy. The most probable charge obtained from the mass number is near the N/Z of both projectile and composite system which corresponds to the quasi elastic and deep inelastic reactions, respectively [45].

An intermediate composite system has been shown as the result of a complete damping of the relative motion between the projectile and target nuclei. The projectile-like fragments are produced via binary nuclear system that collective effects dominate. On the other hand, at high energies, the process is dominated by individual nucleonic collisions that described as participant-spectator models. The values of most probable charge distinguish the reaction mechanisms to produce the projectile-like fragments.

At intermediate energies, D.Guerreau et al. [46] reported the observation of the systematic shift of isotope distributions between two targets. The isotope distributions of fragment yield were measured in $^{40}\text{Ar}+\text{Ni}$ and $^{40}\text{Ar}+\text{Au}$ reactions at 44A MeV. The systematic shift of the isotope distributions for a given element of Si in $^{40}\text{Ar}+\text{Au}$ reaction was observed about 0.3 mass unit towards the neutron rich side. However, their result is different from our data. The fitting results of our charge distributions have shown no significant difference of $Z_{prob}(\text{EXP})$ between the Be and Ta targets.

We have already found that the factorization assumption is invalid for production of neutron-rich nuclei. The flexibility of the charge distribution except the most probable charge is the slope parameter. Thus, we would seek for the origin of target dependence in the slope constant U . Due to the BOF, the U may change from a simple constant to a complex parameter which depends on target nuclei.

As the target dependence of Z_{prob} has not been found, we assume now that the Z_{prob} can be described as the EPAX formula for both of the targets. We make an attempt to fit the data with the function of charge distribution. Fitting parameters were U in neutron-rich side and mass yield Y , and fragment mass dependence of U is

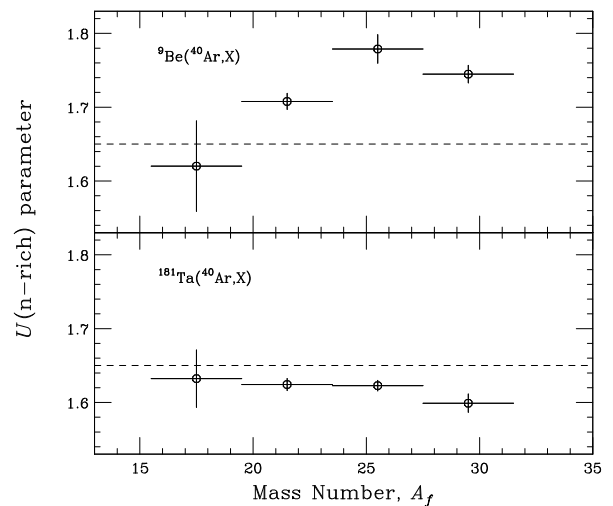


FIG. 16: U parameters as a function of fragment mass for the production targets of Be and Ta. On the assumption that the value of U is same for every group of four sets of A_f data, the fitting results are shown with the systematic error. The dashed lines are the values of $U=1.65$ from the EPAX.

tried to be obtained. The fitting procedure is performed for the data of each fragment-mass group, where every 4 mass units are combined to avoid poor statistics.

Figure 16 shows the U parameters as a function of fragment mass for both targets. We plot the values with the systematic errors. The slope parameter U of EPAX is a constant of 1.65 (dashed lines). The average of U is 1.62 for the Ta target. The smaller U gives larger values of production cross sections for neutron-rich nuclei. On the other hand, the U parameter of Be target is larger than 1.65 and shows fragment mass dependence. Our data demonstrate the BOF for very neutron-rich nuclei as the target dependence of U parameter.

2. Predictive power of new parametrization

We have obtained the modified EPAX formula for the nuclear fragmentation at an intermediate energy for both Be and Ta targets. To confirm the validity of our parametrization, we show an example of the production cross section predicted for extremely neutron-rich nuclei. Figure 17 shows the predictive power of the new parameterization. The dashed and solid curves are the charge distribution of mass-24 isobars produced in $^{40}\text{Ar}+^9\text{Be}$ and $^{40}\text{Ar}+^{181}\text{Ta}$ reactions, respectively. The solid box is the cross section of fragmentation channel for $^{181}\text{Ta}(^{40}\text{Ar}, ^{24}\text{O})$. This value acquired in another experiment [47] is in agreement with our new parametrization clearly.

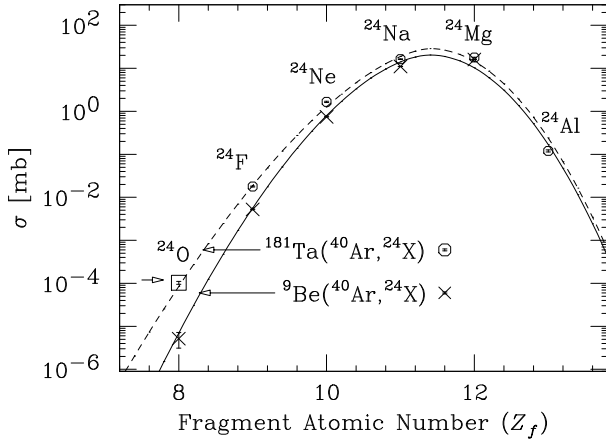


FIG. 17: Predictive power of cross sections of the new parametrization. The solid box is the data of ^{24}O with a tantalum target.

G. Mechanism of Prefragment Production

We have investigated the nuclear fragmentation reaction in nucleus-nucleus collisions at intermediate energies. The momentum distributions of projectile-like fragments have been measured for various isotopes including very neutron-rich nuclei. The charge distributions of fragment cross sections acquired with the Be and Ta targets have revealed the BOF for very neutron-rich nuclei. In order to explain the origin of BOF, we discuss the mechanism of prefragment production in terms of the AA model. In the AA model, the production cross section of a final fragment is determined by the charge distribution and the excitation energy of prefragments.

First, we discuss the charge distribution of prefragments on the basis of AA model. The abrasion model is a macroscopic description which gives a picture of a clean cut of the projectile nucleus by the target nucleus [48]. The concept of geometrical separation in an overlap or participant zone does not specify its proton-to-neutron ratio. A few different methods to calculate the charge distribution of the prefragments are so far proposed, a correlation model [49], hypergeometrical model [50], and GDR model [51]. After all, the charge distribution of prefragments from these methods depends on the projectile nuclei but has no target dependence.

Next, we discuss the excitation energy of prefragments. In an early model [52], the average excitation energy of a prefragment after abrasion was estimated from the additional surface energy due to the excess surface area. Several studies have been made on the source of the excitation energy [8, 53, 54]. According to the researches, the surface energy is not the main source of the excitation energy, but, one of the energy sources for prefragment excitation. At least, the target dependence of the excitation energy can be seen in the surface energy. Figure 18 shows a schematic view of prefragment production. The prefragments of the same mass number A_f' are produced

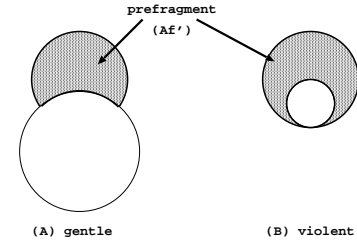


FIG. 18: A schematic drawing of prefragment production. The prefragments of the same mass number (A_f') are produced by projectile fragmentation reaction with target nuclei of different nuclear radius. For the large impact parameter leads to (A) gentle reaction, and (B) violent reaction is expected for the small impact parameter with the small target nuclei.

by the projectile fragmentation reaction with target nuclei of different nuclear radius. If a target nucleus has a large size, the impact parameter is also large to produce the prefragment (case A). On the other hand, the small size of a target nucleus caused the violent collision to form the prefragment with the same mass number (case B). In the geometrical model, we calculated the surface energy of prefragments in Ar+Be and Ar+Ta reactions. As the result, large difference of E_s is presented for both of the targets. As for the prefragments of $\Delta A = 20$, the values of E_s are approximately 90 MeV and 10 MeV for the Be and Ta targets, respectively. The target dependence of prefragment excitation energies stems from the additional surface energies in the AA model.

We observed no significant target dependence of momentum peak shift in the data for the projectile-like fragments of $A_f \geq 20$. Assumed that nucleons are emitted homogeneously from the hot prefragment in the ablation process, the velocity of a prefragment does not change on average when it becomes the final fragment. The results of momentum peak shift show that the energy losses in the fragmentation process for the fragment of $\Delta A = 20$ were 60~80 MeV for both of the targets. The energy losses are not correlated to the additional surface energies on the calculation. Thus, we cannot deny the possibility that the BOF originates from the target dependence of the charge distributions for prefragments except the excitation energies.

To apply this idea to the BOF problem, we suggest two mechanisms of a fluctuation giving for the charge distributions of prefragments. One is the nucleon exchange process during the fragmentation process, and another is the effect from the difference of nucleon-nucleon total cross sections (σ_{pp}, σ_{nn} and σ_{pn}).

We observed the nucleon exchange process during the fragmentation process in our data. The fitting results of P_0 and σ_H carry the information at the abrasion stage and supporting that “pure” projectile fragmentation is a dominant process at intermediate energies. As for σ_L , the larger values of σ_L than σ_H may be related to the energy loss due to the transfer process. Unlike the be-

havior of σ_H , σ_L has a linear dependence as a function of fragment mass. The linear dependence may be connected from both projectile and target nuclei. So, the source of transferred nucleons can be assumed to be the participant region. Since the Ta target nucleus is more neutron-rich than the Be, the probability of neutron transfer should be large. The nucleon exchange reaction between projectile and target nuclei during the abrasion process may break the factorization of fragment production cross sections.

The difference of the total cross sections between proton-to-proton (σ_{pp}) and proton-to-neutron (σ_{pn}) may bring the fluctuation of prefragment charge distributions. As a fact known well, the σ_{np} is larger than the σ_{nn} and σ_{pp} when the nucleon energy is less than 500 MeV. In projectile fragmentation process, a neutron-rich target nucleus easily knocks out protons in the projectile nucleus, so that the production of neutron-rich prefragments is promoted.

The discussions so far are qualitative. However, they gives several predictions. First, if the nucleon exchange process is just the reason of BOF, the probability of nucleon exchange reaction becomes large at low energies. The nuclear fragmentation experiments with lower incident beam energies than at our experiment may reveal the large BOF effect for very neutron-rich nuclei. Secondly, if the difference of N-N reaction cross sections causes the BOF, the nuclear fragmentation experiment with 100-800A MeV beams should be carried out to confirm the BOF for very neutron-rich nuclei. Since the cross section curves of σ_{pp} and σ_{pn} cross at 500A MeV, the difference of U-parameter between the Be and Ta targets might change to be reversed. The further investigations of fragmentation cross sections at around 500A MeV are of great interest.

V. SUMMARY AND CONCLUSION

The projectile fragmentation reactions at intermediate energies have been investigated using a 90-94A MeV

^{40}Ar beam at RIKEN-RIPS. We paid our attention to the target dependence. Measurement of longitudinal momentum distributions of projectile-like fragments within a wide range for fragment mass and its charge including very neutron-rich nuclei has been performed with ^9Be and ^{181}Ta targets. From the momentum distribution of fragments, a parabolic mass dependence of momentum peak shift was observed in the data of both targets, and a phenomenon of fragment acceleration was observed only in the Be-target data. A linear dependence of the low momentum tail as a function of removed nucleons was found for both targets. As a possible origin of the low momentum tail, we suppose the nucleon exchange reaction. We observed large target dependence of the cross sections to produce very neutron-rich nuclei with $(Z_\beta - Z_f) \geq 2$. The deviation shows that the production cross sections of very neutron-rich nuclei far from the stability line do not factorize. The reaction mechanism was discussed, however the discussions so far are qualitative. It is much interesting to investigate the target dependence of the cross sections at higher energies.

Acknowledgments

The authors wish to thank the RIKEN Ring Cyclotron staff and crew for their cooperation. We are also indebted to Dr. A.G. Artukh, Dr. G.A. Souliotis, and Prof. T. Shimoda for stimulating discussions. One of the authors (M.N.) acknowledges the financial support of the RIKEN Special Researchers' Basic Science Program.

-
- [1] J.A. Winger et al.: Nucl. Instr. Meth. B70, 380 (1992).
 - [2] N. Iwasa et al., Nucl. Instr. Meth. B126, 284 (1997); Th.Schwab, GSI Report No. 91-10 (1991).
 - [3] K. Sümmerer and B. Blank: Phys. Rev. C **61**, 034607 (2000).
 - [4] H. Sakurai et al., Phys. Lett. B **448**, 180 (1999).
 - [5] H. Sakurai et al., Phys. Rev. **C54**, R2802 (1996).
 - [6] M. Notani et al., Phys. Lett. B **542**, 49 (2002).
 - [7] H. Sakurai et al., Nucl. Phys. **A616**, 311 (1997).
 - [8] J.J. Gaimard and K.H.Schmidt: Nucl. Phys. A **531**, 709 (1991).
 - [9] J.R. Cummings et al.: Phys. Rev. C **42**, 2530 (1990).
 - [10] D. Guerreau et al.: Phys. Rev. C **41**, 937 (1990).
 - [11] H.H. Heckman et al.: Phys. Rev. Lett. **28**, 926 (1972).
 - [12] A.S. Goldhaber: Phys. Lett. **53B**, 244 (1974).
 - [13] L. Tassan-Got et al.: Nucl. Phys. A **524**, 121 (1991).
 - [14] T. Kubo et al.: Nucl. Instrum. Methods Phys. Res. B **70** (1992) 309.
 - [15] H. Kumagai et al.: Nucl. Instrum. Methods Phys. Res. A **470** 562 (2001).
 - [16] B. Robinet et al., Nucl. Instr. Meth. 190, 197 (1981).
 - [17] R. Pfaff et al.: Phys. Rev. C **51**, 1348 (1995).
 - [18] D. Bazin et al.: Nucl. Phys. A **515**, 349 (1990).
 - [19] Ch. O. Bacri et al.: Nucl. Phys. A **555**, 477 (1993).
 - [20] K. Van Bibber et al.: Phys. Rev. Lett. **43**, 840(1979).
 - [21] R. Dayras et al.: Nucl. Phys. A **460**, 299 (1986).
 - [22] J.P. Dufour et al.: Nucl. Instrum. Methods Phys. Res. A **248** (1986) 267.
 - [23] T. Enqvist et al.: Nucl. Phys. A **658**, 47 (1999).
 - [24] D.E. Greiner et al.: Phys. Rev. Lett. **152**, 35 (1975).

- [25] J.B. Cumming et al.: Phys. Rev. Lett. **44**, 17 (1980).
- [26] J.B. Cumming et al.: Phys. Rev. C **24**, 2162 (1981).
- [27] S.B. Kaufman et al.: Phys. Rev. C **26**, 2694 (1982).
- [28] D.J. Morrissey et al.: Phys. Rev. C **39**, 460 (1989).
- [29] V. Borrel et al.: Z.Phys. A **314**, 191 (1983).
- [30] V. Borrel et al.: Z.Phys. A **324**, 205 (1986).
- [31] B. Mottelson : "Nuclear Structure" in Cours de l'Ecole d'Eté de Physique Théorique des Houches (1958).
- [32] F. Auger et al.: Phys. Rev. C **35**, 190 (1987).
- [33] D. Guerreau et al.: Nucl. Phys. A **447**, 37 (1985).
- [34] M.C. Mermaz et al.: Z.Phys. A **324**, 217 (1986).
- [35] A.G. Artukh et al. : Nucl. Instrum. Methods Phys. Res. A **426** (1999) 605.
- [36] C. Grégoire and B. Tamain: Ann. Phys. Fr. **11**, 323 (1986).
- [37] D. J. Olson et al.: Phys. Rev. C **28**, 1602 (1983).
- [38] K. Sümmerer et al.: Phys. Rev. C **51**, 1348 (1990).
- [39] P. Marmier and E. Sheldon : *Physics of Nuclei and Particles* (Academic, New York and London), Vol.I, 15 (1971).
- [40] R. Silberberg and C.H. Tsao: Astrophys. J. Suppl. **25**, 315 (1973).
- [41] R. Silberberg et al. : Astrophys. J. Suppl. **58**, 873 (1985).
- [42] S. Kox et al.: Phys. Rev. C **35**, 1678 (1987).
- [43] M. Buenerd et al.: Nucl. Phys. A **424**, 313 (1984).
- [44] J. Galin : J. Phys. C **5**, **37**, 83 (1976).
- [45] M. Lefort and Ch. Ngô: Ann. Phys. **3**, 5 (1978).
- [46] D. Guerreau et al.: Phys. Lett. **131B**, 293 (1983).
- [47] Y. Yanagisawa et al.: Phys. Lett. B **566**, 84 (2003).
- [48] J. Gosset et al. : Phys. Rev. C **16**, 629 (1977).
- [49] G.D. Westfall et al. : Phys. Rev. Lett. **43**, 1859 (1979).
- [50] W.A. Friedman: Phys. Rev. C **27**, 569 (1983).
- [51] D.J. Morrissey et al.: Phys. Rev. C **18**, 1267 (1978).
- [52] J.D. Bowman et al.: LBL Report **LBL-2908** (unpublished) (1973).
- [53] J.W. Wilson et al.: Nucl. Instrum. Methods Phys. Res. B **18** 225 (1987).
- [54] J. Hüfner et al. : Phys. Rep. **125**, 129 (1985).